Supporting Information

A Flexible Piezoelectret Actuator/Sensor Patch for Mechanical Human-Machine Interfaces

Junwen Zhong[1†], Yuan Ma[1†], Yu Song[1,2], Qize Zhong[4], Yao Chu[1,3], Ilbey Karakurt[1], David B. Bogy[1], and Liwei Lin[1,3*]*

[1] Mechanical Engineering Department, University of California, Berkeley, California, 94720, USA.

[2] State Key Laboratory of Transducer Technology, Institute of Electronics, Chinese Academy of Sciences, Beijing 100190, China.

[3] Tsinghua-Berkeley Shenzhen Institute, Shenzhen, 518055, China.

[4] Temasek Laboratories (TL@ NTU), Nanyang Technological University, 637553, Singapore.

[†] These authors contributed equally to this work.

[*] Correspondence to: junwenzhong@berkeley.edu and lwlin@berkeley.edu

Supplementary Figures

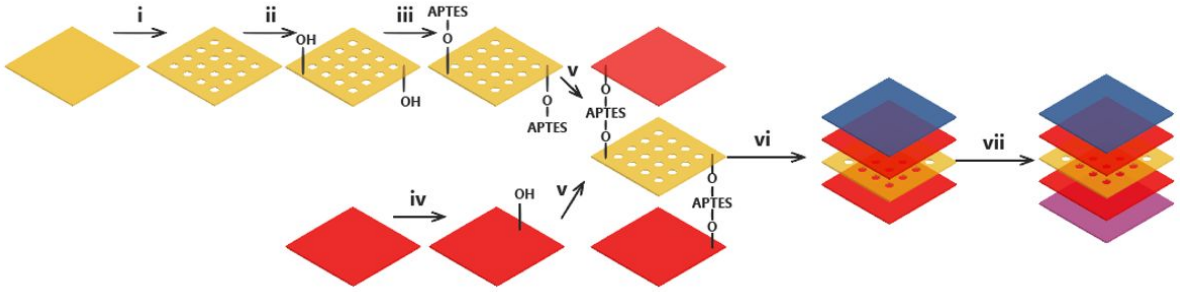

Figure S1. Schematic diagram depicting the fabrication steps for the sandwich-structured piezoelectret: **i:** punching holes on the Ecoflex film; **ii:** O_2 plasma treatment of the Ecoflex film; **iii:** APTES treatment; **iv:** O_2 plasma treatment of the FEP film; **v:** bonding of the sandwich-structured piezoelectret patch; **vi:** Corona charging process; **vii:** top and bottom electrode deposition processes.

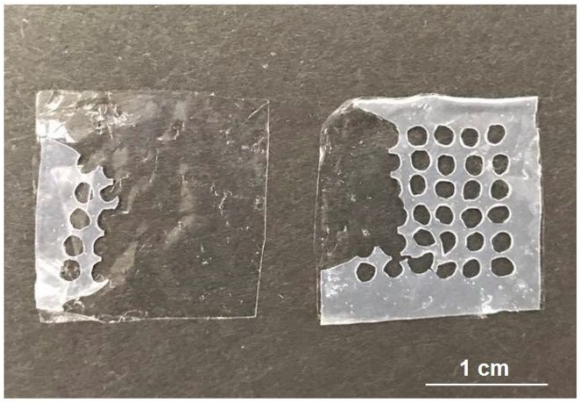

Figure S2. An optical photo of the two FEP films showing the bonding result between the FEP films and Ecoflex spacer is strong, as evidenced by the presence of Ecoflex debris on both FEP films after forcefully breaking the sandwich-structured piezoelectret patch.

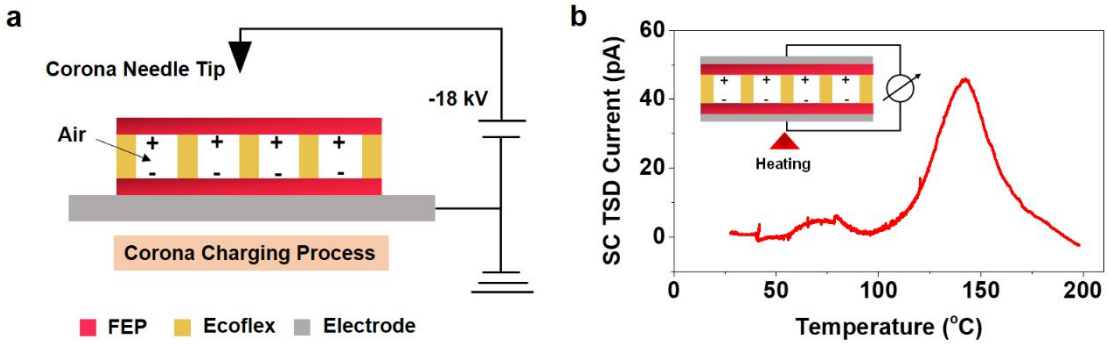

Figure S3. (a) Schematic diagram depicting the corona charging process for the sandwich-structured piezoelectret patch. (b) Thermally stimulated depolarization (TSD) current results for a sandwich-structured piezoelectret patch after the corona charging process. Inset shows the setup for the TSD test.

Corona charging process: The corona charging set-up is used to create surplus charges for the formation of electrical dipoles and it consists of a high voltage power source, a corona needle, and a ground electrode. Samples are placed atop the ground electrode and situated 1 cm below the corona needle tip. High voltage of -18 kV is applied to the corona needle and the air in the cavities of the sandwiched structure can be broken-down for the charging process. The generated free charges are subsequently captured by the inner surfaces of the two FEP films. The long-term retention of charges is maintained owing to the excellent properties of FEP as an electret material. The resulting positive and negative surplus charges on the separate FEP film layers constitute the megascopic electrical dipoles.

TSD test: The short-circuit thermally stimulated depolarization (TSD) technique has been employed to characterize the megascopic electrical dipoles inside the sandwich-structured piezoelectret patch. Both outside surfaces of the patch are metallized with gold (Au) electrode

and then put into a thermal chamber (DH-TSC). The generated outward current heated in the thermal chamber with temperature rising rate of 3 °C/min is measured by a current meter (Keithley 6517B).

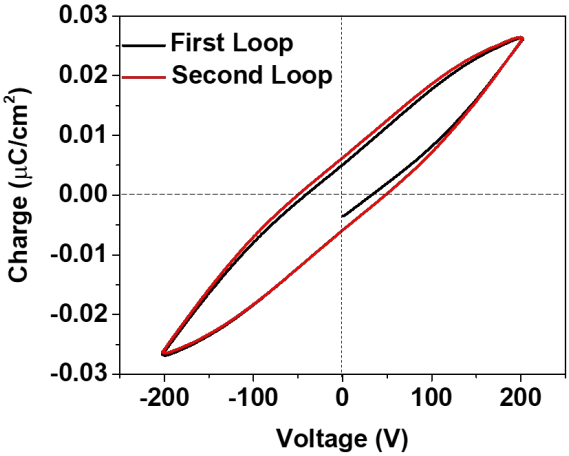

Figure S4. Polarization-electric field (PE) loop for 150 μm thick sandwich-structured piezoelectret, with Hysteresis Period of 100 ms.

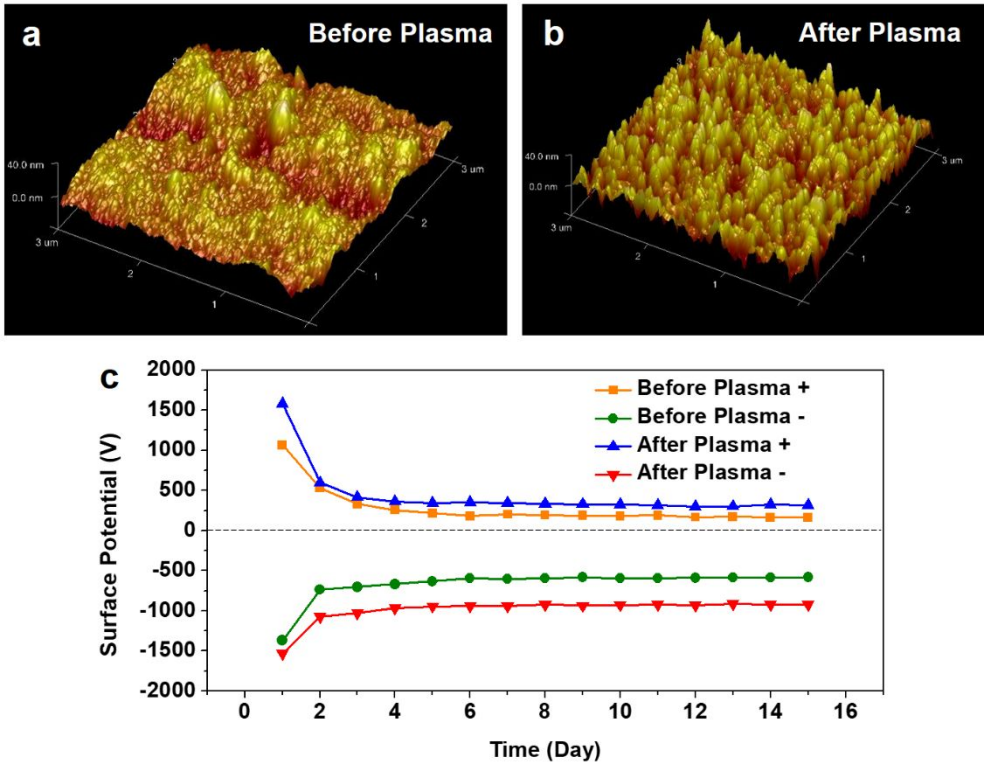

Figure S5. Atomic Force Microscope (AFM) images for the FEP electret films (a) before and (b) after O_2 plasma treating. (c) Surface potential *vs.* time curves for four types of FEP electret films: without the O_2 plasma treatment and positively-charged (orange), without the O_2 plasma treatment and negatively charged (green), with the O_2 plasma treatment and positively charged (blue), and with the O_2 plasma treatment and negatively charged (red).

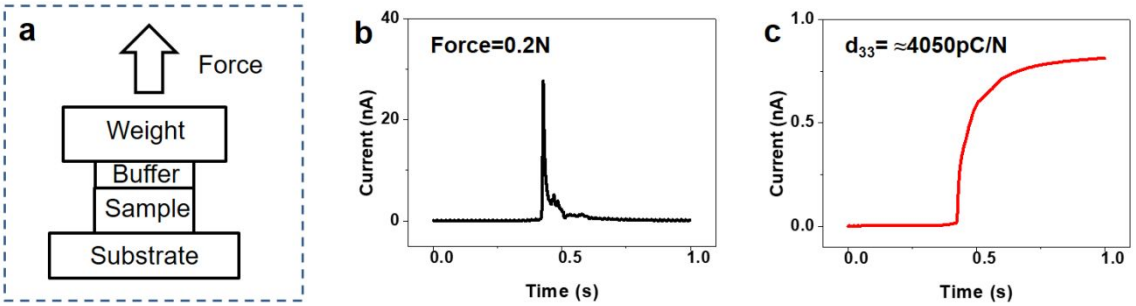

Figure S6. (a) Schematic diagram depicting the process for the measurement of equivalent d_{33} coefficients. (b) The current *vs.* time curve; and (c) corresponding transferred charges computed *via* the integration from the current *vs.* time curve in (b) measured with a prototype sandwich-structured piezoelectret patch.

Equivalent piezoelectric coefficients (d_{33}) measurement: The equivalent piezoelectric coefficient d_{33} (pC/N) is characterized and the first and second subscripts represent the direction of the electric field and applied force, respectively. Samples are first coupled with a soft buffer layer and then pressed by a balance weight and the force (F) applied on the sample is noted. Quickly applying the weight generates a peak response current. By integrating the response current with time, the transferred charge (Q) is calculated to determine the equivalent d_{33} coefficient by the following equation:

$$d_{33} = Q/F \quad (1)$$

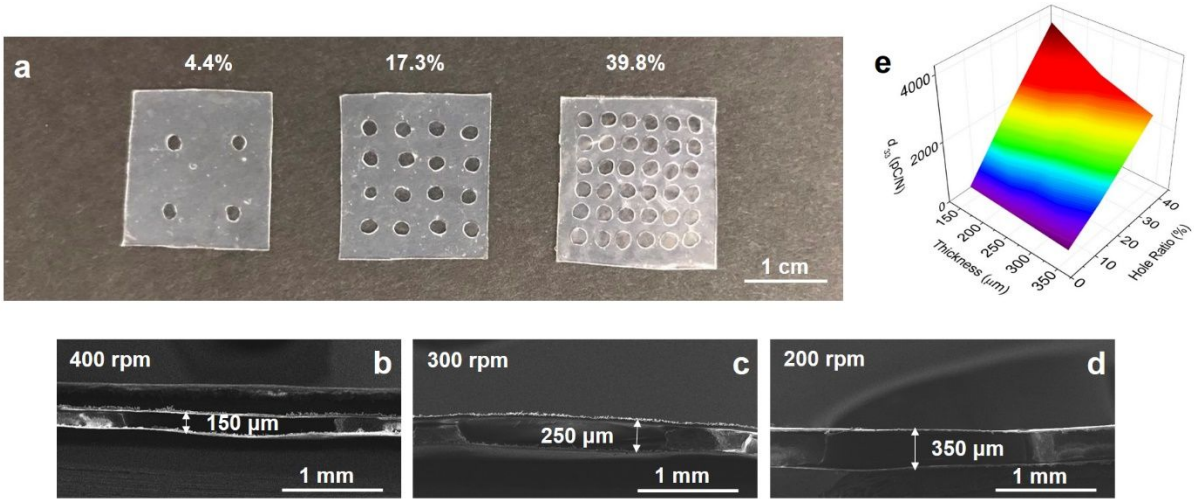

Figure S7. (a) An optical photo showing various sandwich-structured piezoelectret films with cavity to spacer area ratios of 4.4%, 17.3% and 39.8%, respectively. The cross-sectional SEM image are the sandwich-structured piezoelectret patches fabricated by the spinning coating speeds of (b) 400 rpm, (c) 300 rpm and (d) 200 rpm, respectively, for the Ecoflex layer. (e) Measured equivalent piezoelectric coefficients (d_{33}) with different thicknesses of the Ecoflex layer and different cavity to spacer area ratios. As expected, thinner thickness of the Ecoflex layer and larger cavity to spacer area ratio are in favor of higher piezoelectric constants.

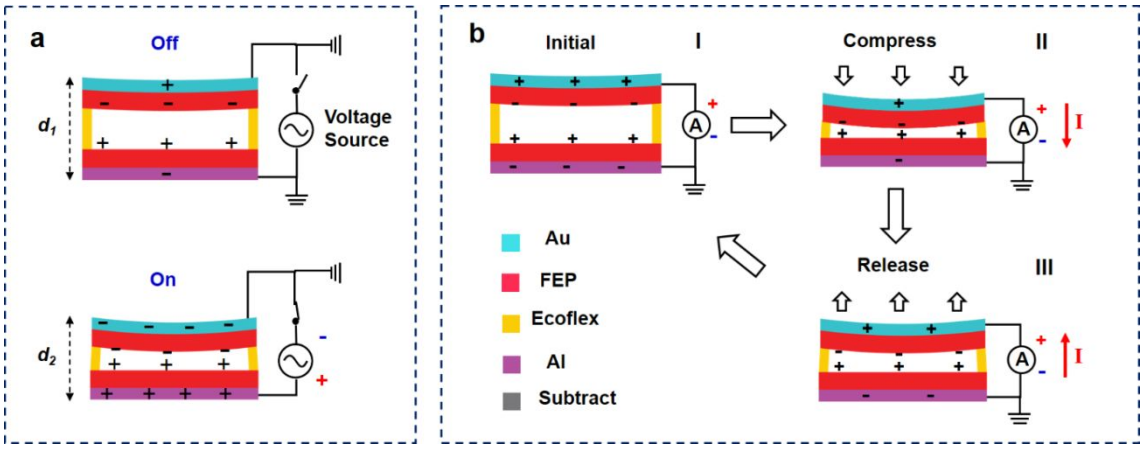

Figure S8. (a) Schematic diagram of the actuator function by applying a bias voltage off and on, respectively. (b) Schematic diagram depicting the sensor function at: (I) initial, (II) compressing, (III) releasing states, respectively.

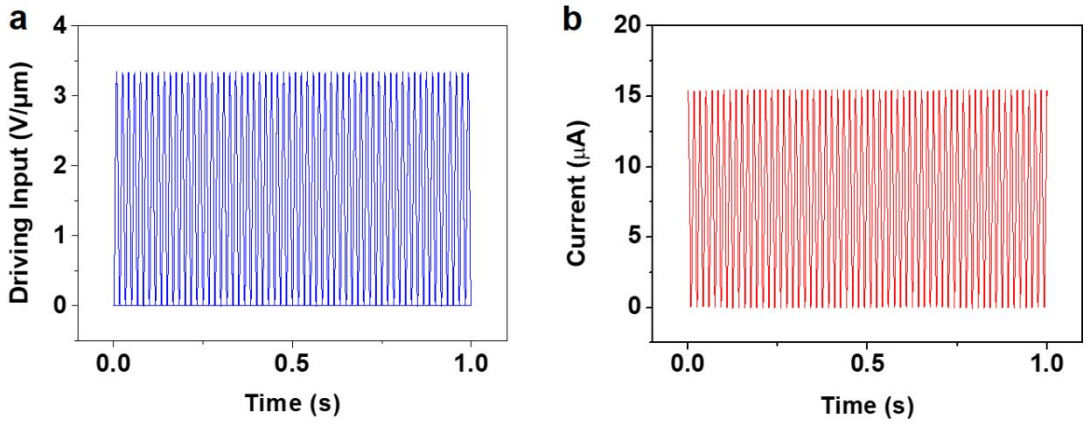

Figure S9. (a) The applied AC driving voltage at a frequency of 60 Hz between 0 to 500 V on a prototype actuator (3.3 V/μm and the whole actuator thickness is 150 μm), and (b) the corresponding current (peak value of 16.5 μA). The peak power consumption of this actuator is about 8.25 mW.

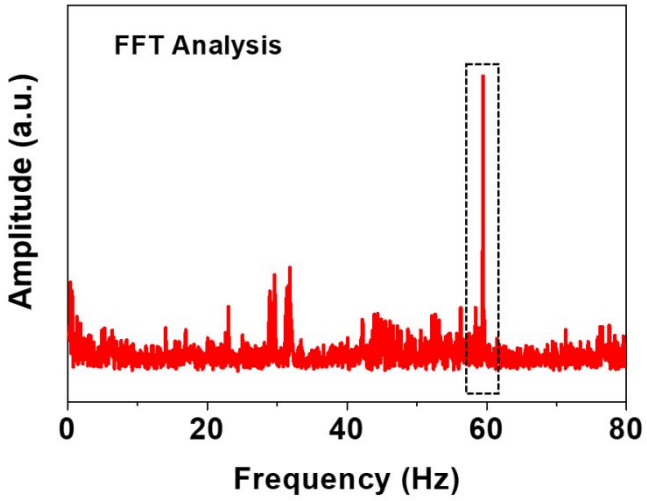

Figure S10. FFT (fast Fourier transform) analysis for the generated force *vs.* time curves under a driving voltage of 500 V (3.3 V/μm). The frequencies of input voltage and output force signal have consistent values at 60 Hz.

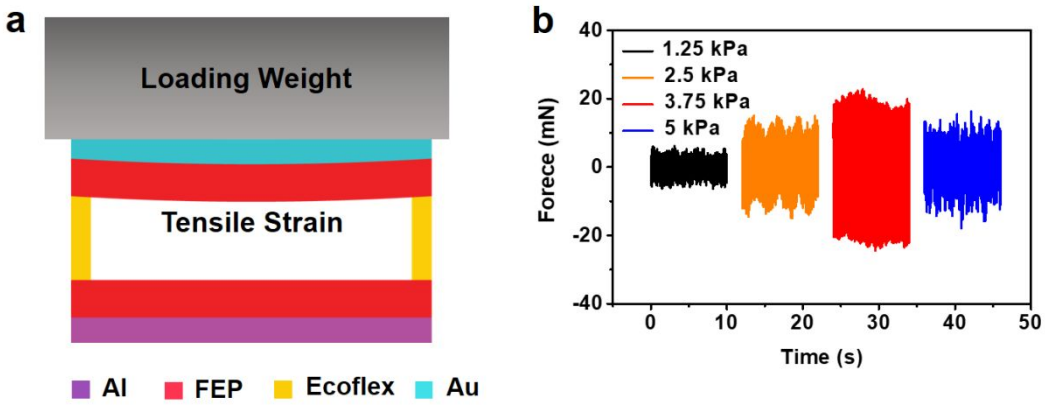

Figure S11. (a) Schematic diagram indicating the applied weight on the actuator by the loading piece on top. (b) The generated force *vs.* time results for the actuator of a standard sandwich-structured piezoelectret patch under increased pre-load pressure from 1.75, 2.5, 3.75 to 5 kPa under a driving voltage of 500 V (3.33 V/μm) at 60 Hz. The magnitude of the external load will impact the output force. Too large external load will affect the vibration of the FEP membrane of our actuator.

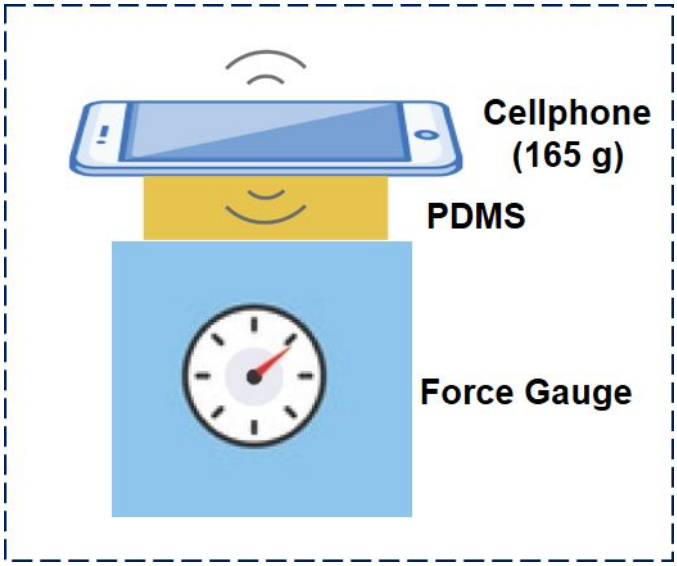

Figure S12. Schematic diagram for the setup of force measurements from a cellphone at its vibration mode with the weight of 165 g.

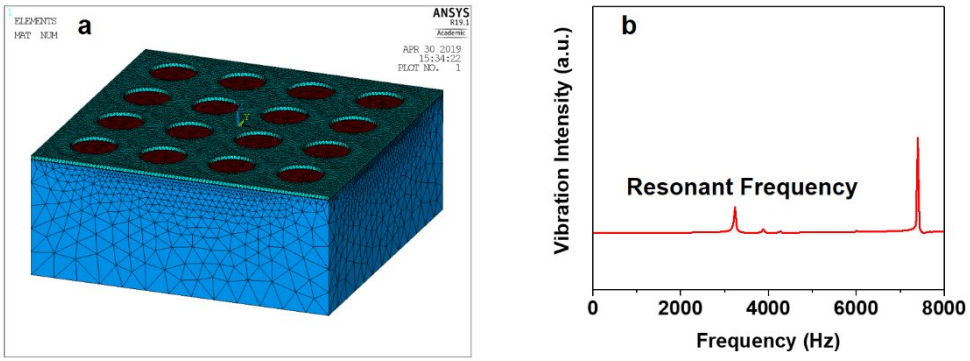

Figure S13. (a) Schematic diagram showing our sandwich-structured piezoelectret device on top of a 5 mm-thick human tissue by using a Finite Element Simulation program. (b) Simulated resonant frequency, which is as high as about 3 kHz.

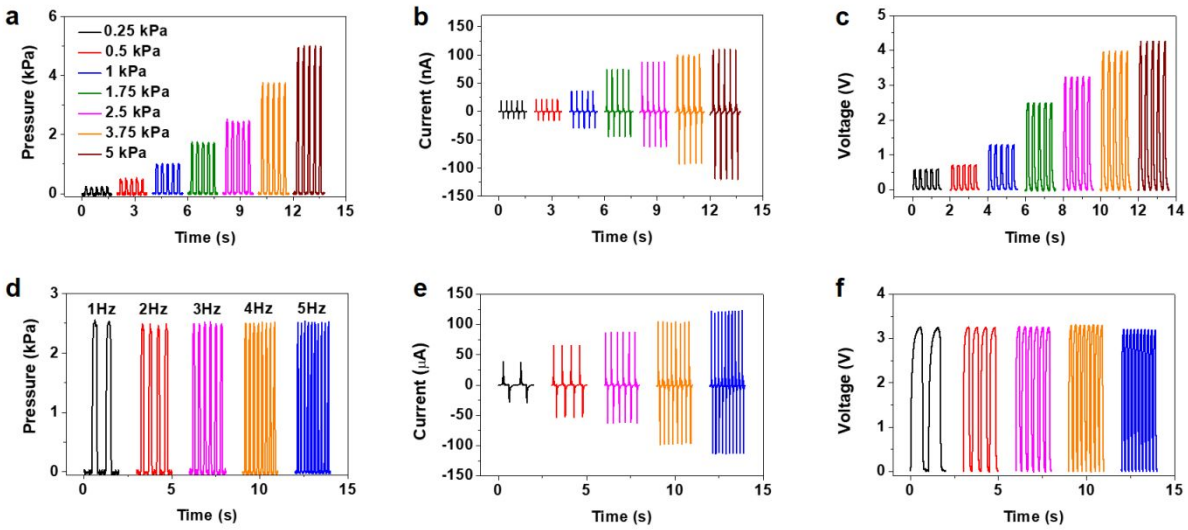

Figure S14. (a) The applied pressure at 3 Hz *vs.* time; (b) short-circuit current *vs.* time sensing results from the standard sandwich-structured piezoelectret patch; and (c) open-circuit voltage *vs.* time sensing results from the standard sandwich-structured piezoelectret patch. (d) The applied pressure of 2.5 kPa with different frequencies *vs.* time; (e) short-circuit current *vs.* time sensing results; and (f) open-circuit voltage *vs.* time sensing results from the standard sandwich-structured piezoelectret patch.

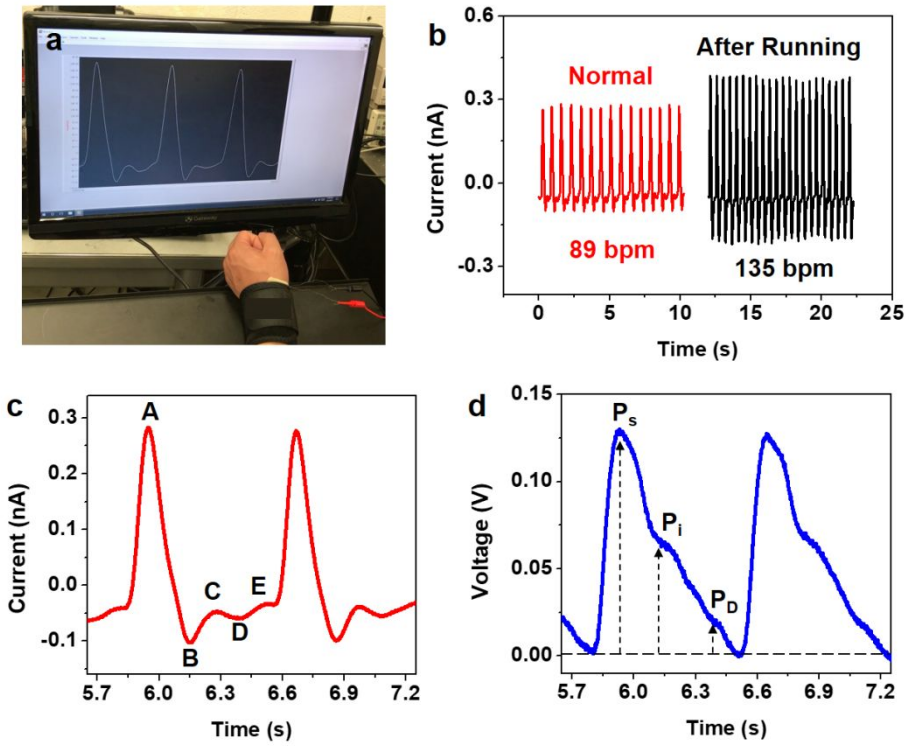

Figure S15. (a) An optical photo depicting a flexible piezoelectret pressure sensor in measuring human arterial pulses. (b) The short-circuit current measurement results for the arterial pulses of a 29-years-old man at normal and excited states. (c) An enlarged view of short-circuit current signals showing clear dynamic details of typical human pulses. (d) An enlarged view of open-circuit voltage signals showing clear static details of typical human pulses.

Notes: As illustrated in **Figure S15a**, a flexible piezoelectret pressure sensor is assembled with a wristband to measure human arterial pulse signals at the wrist. For a 29-year-old male subject, the sensor reveals 89 bpm (beats per minute) heartbeat rate, as shown in **Figure S15b**. After the male subject conducts a running exercise for 10 min, the pulse sharply increases to 135 bpm. Furthermore, the dynamic details of the pulse wave of this subject are presented in the enlarged view in **Figure S15c** with clearly visible characteristics of initially positive (A), early negative (B), re-increasing (C), late re-decreasing (D), and diastolic positive (E) signals. The

enlarged view of the open-circuit voltage further depicts the static details of the pulse wave of this subject (**Figure S15d**.) showing visible systolic peak (P_s), point of inflection (P_i), and dicrotic wave (P_D) clearly.

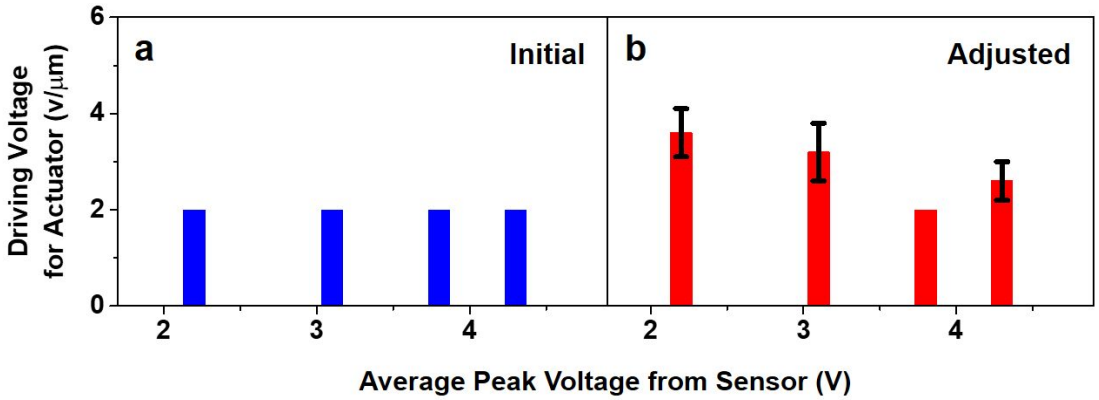

Figure S16. (a) The initial driving voltage for the device with actuator function. (b) The adjusted driving voltage for the device with actuator function to get similar sensation intensity under all pre-load pressure level.

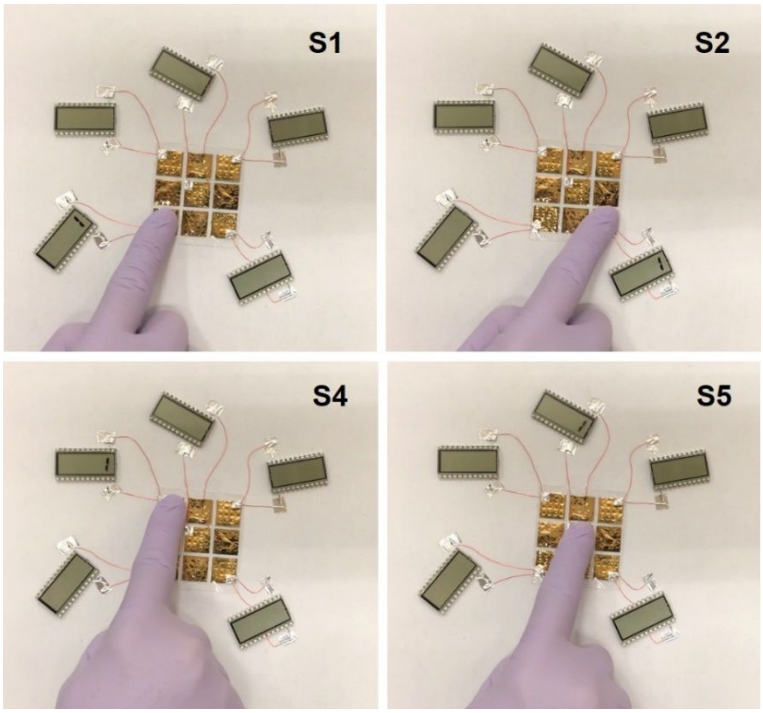

Figure S17. Photo images of the operation of sensor pixels *via* the pushing of a human finger.

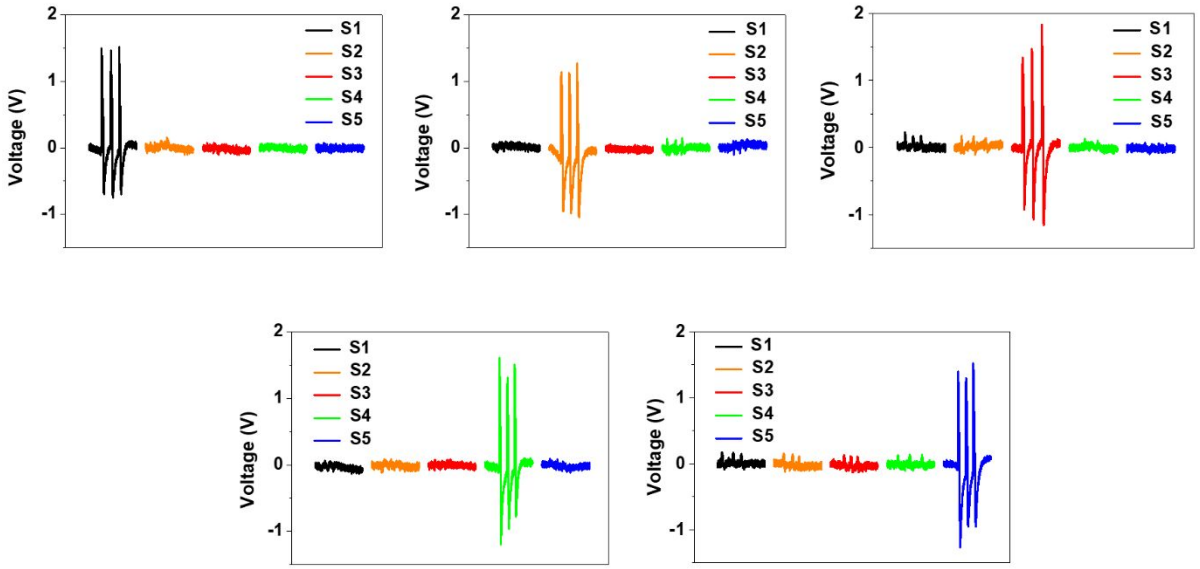

Figure S18. Measured voltage responses from a standard sandwich-structured piezoelectret patch by touching each sensor pixel with the fingertip.

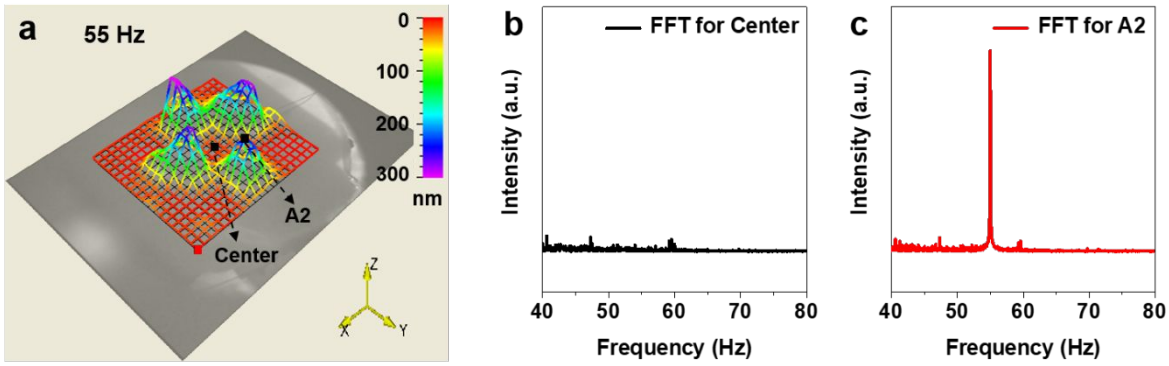

Figure S19. (a) Measured displacement on four actuator pixels under a driving voltage of 200 V (1.33 V/μm) at 55 Hz using the LDV (laser Doppler vibrometer). (b) FFT analysis for the measured LDV results from (cC) a point in the center pixel; and (dD) a point in the actuator pixel #2 (A2).

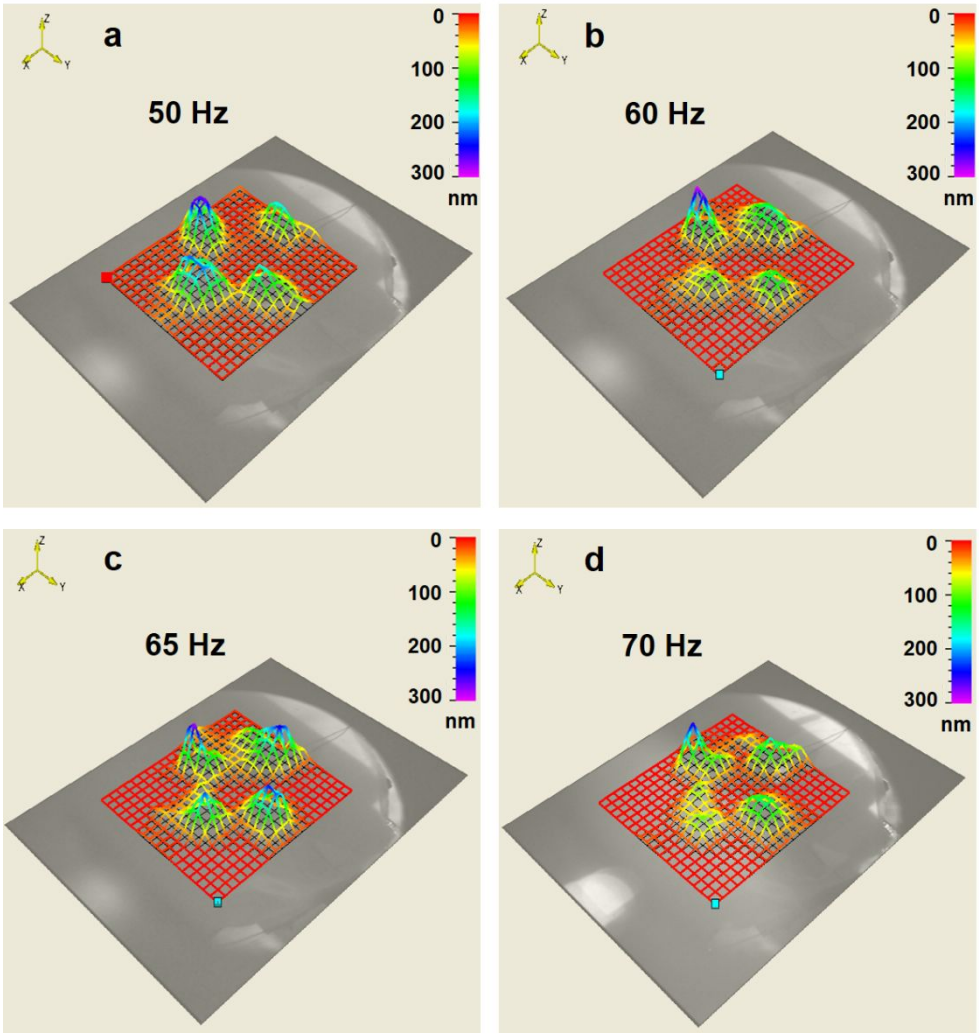

Figure S20. Measured displacement on four actuator pixels under a driving voltage of 200 V (1.33 V/μm) at (a) 50 Hz, (b) 60 Hz, (c) 65 Hz, and (d) 70 Hz, using the LDV (laser Doppler vibrometer).

Table S1. Comparison of the equivalent d_{33} coefficients for piezoelectric and piezoelectret materials/structures

Material	Structure	Piezoelectric Coefficient d_{33}/pC N^{-1}	References
Cellular PP	Film	~205 to 610	1, 2
PDMS Piezolectret	Film	~2000 to 3000	3
PMN-PZT/PT	IDE Structure/Film	~1500 to 2000	4, 5
PZT	Film	~250 to 700	6, 7
$BaTiO_3$	Film	~190	8
PVDF	Film	~33	6
ZnO	Nanowire	~5 to 10	6, 9
FEP Piezoelectret	Film	~1000-3700	10
Sandwich-Structured Piezoelectret	Film	~4050	This Work

(1) Wu, N.; Cheng, X.; Zhong, Q.; Zhong, J.; Li, W.; Wang, B.; Hu, B.; Zhou, J., Cellular Polypropylene Piezoelectret for Human Body Energy Harvesting and Health Monitoring. *Adv. Funct. Mater.* **2015**, *25*, 4788-4794.

(2) Zhong, Q.; Zhong, J.; Cheng, X.; Yao, X.; Wang, B.; Li, W.; Wu, N.; Liu, K.; Hu, B.; Zhou, J., Paper-Based Active Tactile Sensor Array. *Adv. Mater.* **2015**, *27*, 7130-7136.

(3) Wang, J. J.; Lu, C. E.; Lo, S. C.; Su, Y. C.; Fang, W. In *Composite Rubber Electret for Electromechanical Load Detection*, 2017 19th International Conference on Solid-State Sensors, Actuators and Microsystems (TRANSDUCERS), 18-22 June 2017; 2017; pp 1368-1371.

(4) Tang, G.; Yang, B.; Liu, J.-q.; Xu, B.; Zhu, H.-y.; Yang, C.-s., Development of High Performance Piezoelectric d_{33} Mode MEMS Vibration Energy Harvester Based on PMN-PT Single Crystal Thick Film. *Sensor. Actuat. A-Phys.* **2014**, *205*, 150-155.

(5) Li, F.; Lin, D.; Chen, Z.; Cheng, Z.; Wang, J.; Li, C.; Xu, Z.; Huang, Q.; Liao, X.; Chen, L.-Q.; Shrout, T. R.; Zhang, S., Ultrahigh Piezoelectricity in Ferroelectric Ceramics by Design. *Nat. Mater.* **2018**, *17*, 349-354.

(6) Priya, S.; Inman, D. Energy Harvesting Technologies. In *Piezoelectric Energy Harvesting*; Kim, H., Tadesse, Y., Priya, S., Eds; Springer: Boston, 2009; pp 3-39.

(7) Hwang, G.-T.; Annapureddy, V.; Han, J. H.; Joe, D. J.; Baek, C.; Park, D. Y.; Kim, D. H.; Park, J. H.; Jeong, C. K.; Park, K.-I.; Choi, J.-J.; Kim, D. K.; Ryu, J.; Lee, K. J., Self-Powered Wireless Sensor Node Enabled by an Aerosol-Deposited PZT Flexible Energy Harvester. *Adv. Energy Mater.* **2016**, *6*, 1600237.

(8) Qi, Y.; McAlpine, M. C., Nanotechnology-Enabled Flexible and Biocompatible Energy Harvesting. *Energy Environ. Sci.* **2010**, *3*, 1275-1285.

(9) Wang, Z. L.; Song, J., Piezoelectric Nanogenerators Based on Zinc Oxide Nanowire Arrays. *Science* **2006**, *312*, 242-246.

(10) Zhang, X.; Sessler, G. M.; Wang, Y., Fluoroethylenepropylene Ferroelectret Films with Cross-Tunnel Structure for Piezoelectric Transducers and Micro Energy Harvesters. *J. Appl. Phys.* **2014**, *116*, 074109.

Table S2. Comparison for different types of actuators

Type of Actuator	Material	Actuator Structure	Piezoelectric Coefficient pC N^{-1}	Working Inputs	Working Frequency	Application	Typical Performance	Flexibility	Reference
Piezoelectret	Cellular PP	Film	200-600 d_{33}	10-20 V/μm	0.5-10 KHz	Loudspeaker	SPL: 80-100 dB	Yes	1, 2
Piezoelectret	Stacking cellular PP	Film	750-1500 d_{33}	15-30 V/μm	60-100 kHz	Ultrasound	Sound pressures of about 20 to 40 Pa	No	3
Piezoelectret	Cellular parylene electret	Comb drive	~1500 d_{33}	10-20 V/μm	<200 Hz	MEMS	Maximal peak to peak displacement of 0.4 mm	No	4
Piezoelectric	PVDF	Film/Cantilever	20-30 d_{31}/d_{33}	50-75 V/μm	<3 kHz	Haptic feedback	Applications in wearables and touch screen	Yes	5, 6
Piezoelectric	PVDF-TrFe	Cantilever	135 d_{31}	13 V/μm	<3 kHz	Smart skin	Elastic energy density of 0.13 J/cm^3	Yes	7, 8
Piezoelectric	PZT	Stacked	410 d_{33}	40 V/μm	Resonant frequency at 456 Hz	MEMS	Maximal peak displacement of 16.5 μm	No	9, 10
Piezoelectric	AlN	Cantilever	~2 d_{31}	100 V/μm	10kHz	CMOS compatible MEMS	Peak displacement of 20 nm	No	11, 12
Electrostriction	Stretchable and Transparent ionic conductors	Film	/	10-20 kV (Voltage)	<10 kHz	Transparent Loudspeaker	Maximal area strain over 150%, transparency over 99%	Yes	13
Electrochemical	MoS_2	Cantilever	/	0.6 V (Voltage)	0.0042-0.125 Hz	May have applications in robotics	Strain of 0.8%, Stress of 11-17 Mpa	Yes	14
Thermal expansion	Nylon (6, 6)	Wire	/	0.03 V/μm	<5 Hz	Artificial muscles	Strain of 10%, Stress of 22 MPa	Yes	15
Piezoelectret	Sandwich-structured piezoelectret	Film/Cantilever	4050 d_{33}	0.6-3.3 V/μm	10-1700 Hz	Human interactivity	Peak force about 20 mN, easy to be patterned	Yes	This Work

1. Li, W.; Wu, N.; Zhong, J.; Zhong, Q.; Zhao, S.; Wang, B.; Cheng, X.; Li, S.; Liu, K.; Hu, B.; Zhou, J., Theoretical Study of Cellular Piezoelectret Generators. *Adv. Funct. Mater.* **2016**, *26*, 1964-1974.
2. Sessler, G. M.; Hillenbrand, J., Piezoelectret Microphones: A New and Promising Group of Transducers. *J. Acoust. Soc. Am.* **2006**, *120*, 3272-3272.
3. Hillenbrand, J.; Sessler, G. M., DC-Biased Piezoelectret Film Transducers for Airborne Ultrasound. *Ferroelectrics* **2014**, *472*, 77-89.
4. Feng, Y.; Hagiwara, K.; Iguchi, Y.; Suzuki, Y., Trench-Filled Cellular Parylene Electret for Piezoelectric Transducer. *Appl. Phys. Lett.* **2012**, *100*, 262901.
5. https://www.acoustics.co.uk/pal/wp-content/uploads/2015/11/Properties-of-poled-PVDF.pdf (accessed Oct 9, 2018).
6. https://www.novasentis.com/applications, (accessed Oct 25, 2018).

7. Zhang, Q. M.; Li, H.; Poh, M.; Xia, F.; Cheng, Z. Y.; Xu, H.; Huang, C., An All-Organic Composite Actuator Material with A High Dielectric Constant. *Nature* **2002**, *419*, 284-287.
8. Tomoaki Karaki; chin Chou, I.; Leslie, E. C., Electron-Irradiation Induced Phase Transition in Poly (Vinylidene Fluoride-Trifluoroethylene) Copolymer. *Jpn. J. Appl. Phys.* **2000**, *39*, 5668.
9. Sabri, M. F. M.; Ono, T.; Said, S. M.; Kawai, Y.; Esashi, M., Fabrication and Characterization of Microstacked PZT Actuator for MEMS Applications. *J. Microelectromech. S.* **2015**, *24*, 80-90.
10. Jain, A.; K. J, P.; Sharma, A. K.; Jain, A.; P.N, R., Dielectric and Piezoelectric Properties of PVDF/PZT Composites: A Review. *Polym. Eng. Sci.* **2015**, *55*, 1589-1616.
11. Joseph, C. D.; Bryan, C. P.; Biju, N.; Ravi, M.; Beth, L. P., Aluminum Nitride on Titanium for CMOS Compatible Piezoelectric Transducers. *J. Micromech. Microeng.* **2010**, *20*, 025008.
12. Aluminum nitride (AlN) Piezoelectric Constants, Electromechanical Coupling Factor. In *Group IV Elements, IV-IV and III-V Compounds. Part A - Lattice Properties*, Madelung, O.; Rössler, U.; Schulz, M., Eds. Springer Berlin Heidelberg: Berlin, Heidelberg, 2001; pp 1-4.
13. Keplinger, C.; Sun, J.-Y.; Foo, C. C.; Rothemund, P.; Whitesides, G. M.; Suo, Z., Stretchable, Transparent, Ionic Conductors. *Science* **2013**, *341*, 984-987.
14. Acerce, M.; Akdoğan, E. K.; Chhowalla, M., Metallic Molybdenum Disulfide Nanosheet-Based Electrochemical Actuators. *Nature* **2017**, 5*49*, 370-373.
15. Haines, C. S.; Lima, M. D.; Li, N.; Spinks, G. M.; Foroughi, J.; Madden, J. D. W.; Kim, S. H.; Fang, S.; Jung de Andrade, M.; Göktepe, F.; Göktepe, Ö.; Mirvakili, S. M.; Naficy, S.; Lepró, X.; Oh, J.; Kozlov, M. E.; Kim, S. J.; Xu, X.; Swedlove, B. J.; Wallace, G. G.; *et al.*, Artificial Muscles from Fishing Line and Sewing Thread. *Science* **2014**, *343*, 868-872.

Supporting Videos

Video 1: Vibration of a sandwich-structured piezoelectret patch under a driving voltage of 3.33 V/μm at 10 Hz.

Video 2: Audible sound generated by a sandwich-structured piezoelectret patch under a driving voltage of 3.33 V/μm with driving frequencies from 10 to 1700 Hz.

Video 3: Illuminating LCD pixels composing the number of "1" by tapping a sandwich-structured piezoelectret patch.

Video 4: Measured output current from a sandwich-structured piezoelectret patch by putting a dandelion (0.075 g) on top.

Video 5: The operation of the sensor pixels *via* fingertips.

Supplementary Explanation 1: The simplified model of a sandwich-structured piezoelectret patch as an actuator unit and the performances of the actuator based on the cantilever configuration.

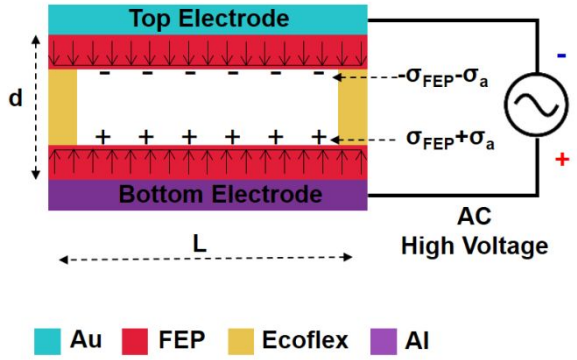

Figure S21. The simplified model of a sandwich-structured piezoelectret patch as an actuator (one working unit).

The simplified model of an actuator (one working unit) based on the sandwich-structured piezoelectret patch is schematically depicted in **Figure S21**. Each air cavity can be regarded as a parallel-plate capacitor. After the corona charging process, the inner surfaces of the FEP films are charged with opposite charges σ_{FEP}. When a driving voltage (V_a) is applied between the two electrodes (Al layer and Au layer), additional charge density σ_a will be accumulated on both electrodes. The combined electric potential (V_0+V_a), where V_0 is the original electrical potential difference between the two electrodes, will exert attractive or repulsive force (f) per unit length on both electrodes towards each other. The distributed electric force, f, applied on each electrode can be expressed as:

$$f = (\sigma_{FEP} + \sigma_a) E = (\sigma_{FEP} + \sigma_a) \frac{V_0 + V_a}{2d} \qquad (2)$$

where d is the distance between the electrodes.

In the working unit, the force between the electrodes is balanced by the deformation of

the Ecoflex spacer layer and the deflection of the FEP/electrode layers. From the force balance equations, the force, F, generated by the Ecoflex layer onto both electrodes is:

$$F = \frac{fL}{2} \tag{3}$$

where L is the total length of the working unit.

The electrical force, F, will deform the working unit. According to equation (3), the σ_{FEP} is a key factor to affect the deformation. A finite element model with dimensions shown in **Figure S22a** is built in ANSYS to perform electrostatic analysis and structural analysis. The electric field and electrostatic force between the electrodes are first calculated through an electrostatic analysis. The force results are then imported to the structural model to solve the deformation data. As indicated in **Figure S22b**, with fixed device thickness (150 μm in the simulation), larger initial σ_{FEP} will contribute to the larger initial displacement, and increasing the driving voltage will increase the displacement value from the initial value. **Figure S22c** shows the displacement vs. time curves for different σ_{FEP} values (0, 0.015, 0.03, 0.06, 0.12, 0.24, 0.5 mC/m^2) under constant driving voltage of 500 V, clearly showing that larger σ_{FEP} will enable the actuator with larger displacement variation.

We also use finite element simulation to investigate the effect of device thickness on driving voltage. Under given σ_{FEP} value (0.03 mC/m^2 in the simulation), decreasing the device thickness (from 300 to 37 μm) by decreasing the Ecoflex spacer layer thickness can significantly lower the driving voltage, as shown in **Figure S22d and S22e**. By decreasing the thickness of the Ecoflex spacer layer, the clearance between the top surface and the bottom surface is reduced. Therefore, under a fixed driving voltage, a stronger electric field and electrostatic force will be produced for the actuator with the thinner Ecoflex spacer layer.

However, if the Ecoflex layer is too thin, the top surface might be in contact with the bottom surface, thus affecting the performance of the actuator. Therefore, an optimum design of the spacer layer (both thickness and the pattern of the holes) is necessary.

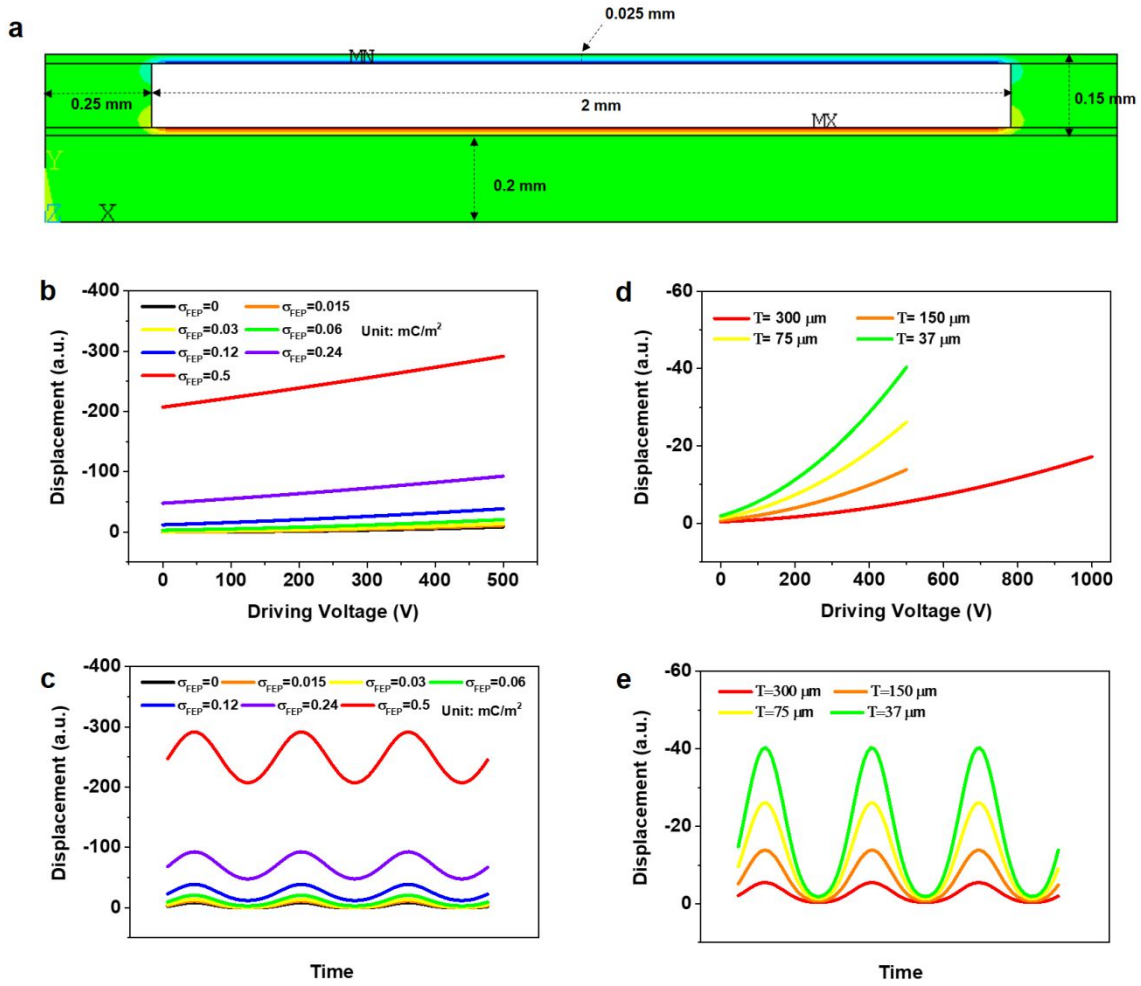

Figure S22. (a) The dimensions of a working unit of piezoelectret actuator for finite element simulation. (b) Displacement vs. driving voltage curves and (c) displacement vs. time curves for given device thickness of 150 μm and different σ_{FEP} value (0, 0.015, 0.03, 0.06, 0.12, 0.24, 0.5 mC/m^2). (d) Displacement vs. driving voltage curves and (e) displacement vs. time curves for given σ_{FEP} value of 0.03 mC/m^2 and different device thickness (300, 150, 75, 37 μm).

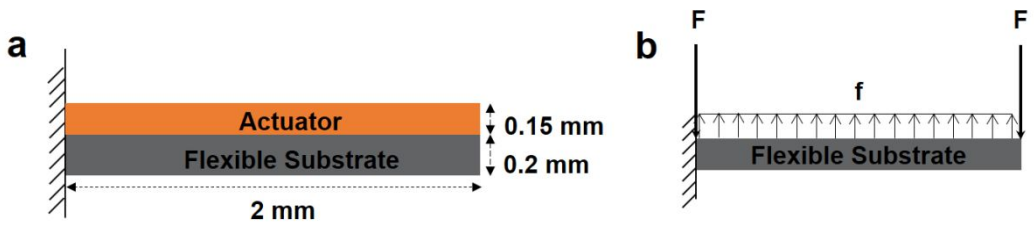

Figure S23. (a) The dimensions of cantilever configuration. (b) A simplified actuator force model based on the cantilever configuration

For cantilever configuration, a flexible substrate is attached on the actuator. As the thickness (2 mm) and the stiffness of the flexible substrate is much larger than that of the FEP/electrodes (25 μm/50 nm) (**Figure 23a,** total thickness of actuator is 0.15 mm), and the Ecoflex and FEP layers are much softer than the flexible substrate, the deflection of the cantilever structured actuator is mostly dominated by the deflection of the flexible substrate. Therefore, the deflection of the actuator can be simplified to a cantilever with uniform load f and a concentrated load F at the end point of the cantilever (**Figure S23b**). The maximum deflection of the cantilever is:

$$\delta = \frac{FL^3}{3EI} - \frac{fL^4}{8EI} = \frac{fL^4}{24EI} \tag{4}$$

where I is the area moment of inertia and E is the Young's Modulus of flexible substrate.

Combining equations (2) and (4), the maximum deflection of the cantilever is at the end of the cantilever as:

$$\delta = \frac{\left(\sigma_{FEP} + \sigma_a\right) L^4 \left(V_0 + V_a\right)}{48dEI} \tag{5}$$

According to equation (5), the deflection δ of the cantilever-structured actuator is linearly correlated to $\frac{\left(\sigma_{FEP} + \sigma_a\right)\left(V_0 + V_a\right)}{d}$. Under a low voltage, the distance between the electrodes

(*d*) does not change significantly and the deflection of the substrate δ increases monotonically with V_a.

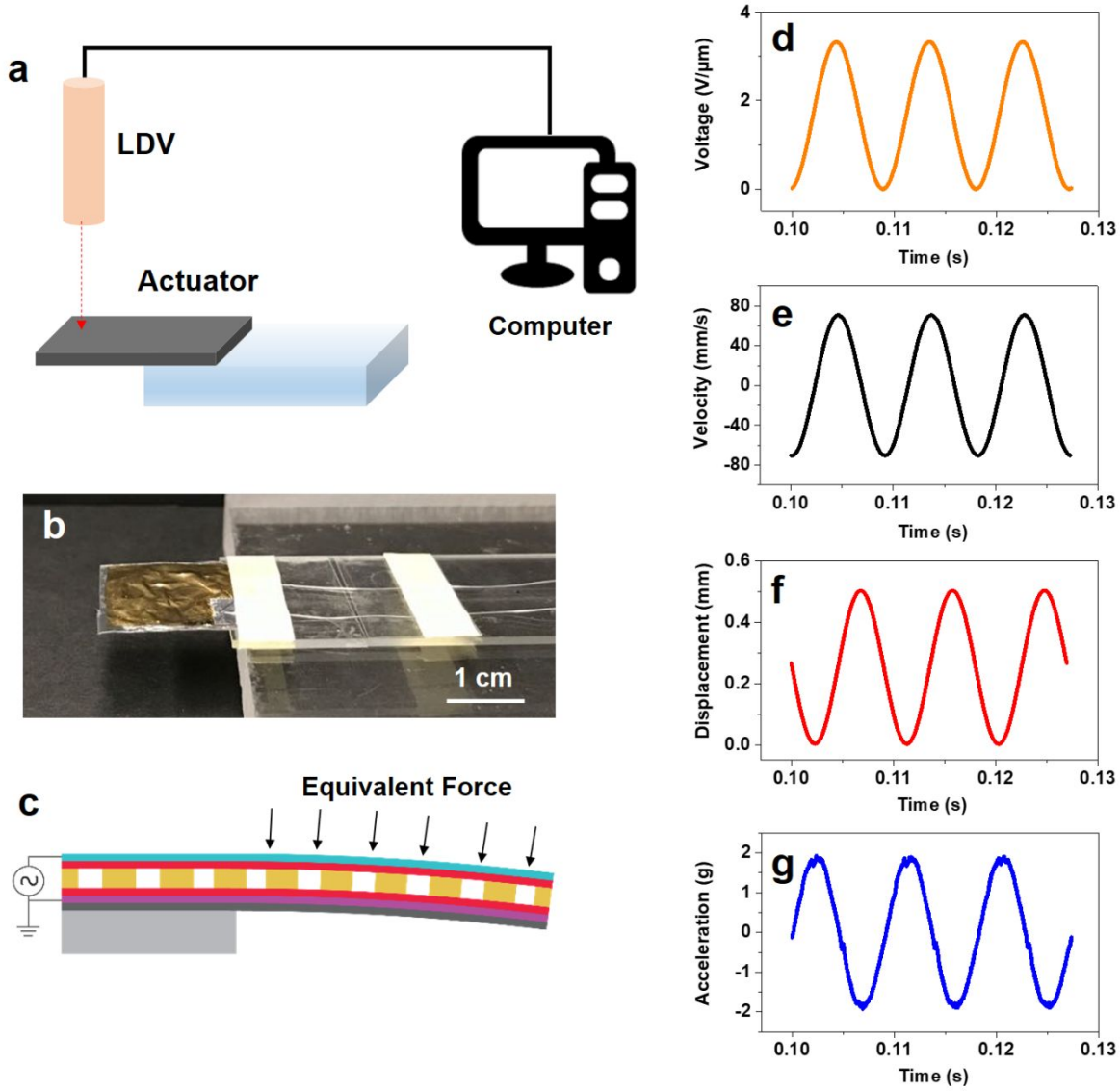

Figure S24. (a) Laser Doppler Velocimetry (LDV) measurement system for characterizing the vibration of an actuator. (b) An optical photo of the actuator with the cantilever configuration. (c) Schematic diagram showing the downward movement at the tip of the cantilever under an applied voltage. (d) The applied voltage *vs.* time curves. (e) The measured velocity *vs.* time results at the tip of the cantilever-structured actuator. (f) The corresponding displacement *vs.* time results for the cantilever-structured actuator. (g) The corresponding acceleration *vs.* time plot.

Experimentally, an LDV is used to characterize the cantilever-structured actuator (**Figure S24a and S24b**). In accordance with the theoretical and simulation results, when a positive driving voltage is applied, the cantilever configuration will bend downward (**Figure S24c**). Moreover, several testing results show the same response trends, such as the applied voltage curves (**Figure S24d**) and the corresponding output results for the actuator, including velocity *vs.* time results (**Figure S24e**), acceleration *vs.* time results (**Figure S24f**), and displacement *vs.* time results (**Figure S24g**).

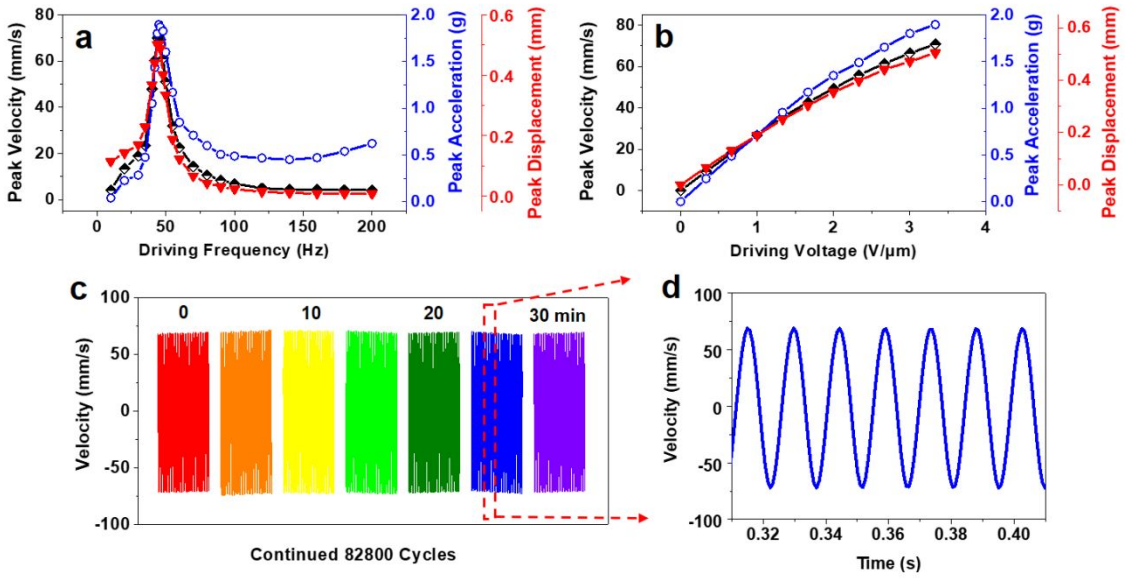

Figure S25. Peak velocity, acceleration and displacement of the cantilever actuator: (a) under different driving frequencies and a constant voltage of 500 V (3.33 V/μm); and (b) under different driving voltages and a constant frequency of 55 Hz. (c) Velocity *vs.* time curves of a cantilever actuator for continuous operation of 30 minutes under a constant driving voltage of 500 V and frequency of 55 Hz. (d) Expanded velocity *vs.* time curves during the stability test.

For a fixed applied driving voltage of 500 V (3.33 V/μm), and varying frequencies from 10 to 200 Hz, the peak values of velocity, acceleration, and displacement of a cantilever-

structured actuator are measured (**Figure S25a**). The velocity, acceleration, and displacement all have maximum magnitudes at about 55 Hz with the values of 70.87 mm/s, 1.89 g and 0.51 mm, respectively, indicating the resonant frequency of the cantilever structure. By fixing the frequency at 55 Hz, the peak displacement, velocity, acceleration increase nearly linearly with respect to the applied voltage (**Figure S25b**). The vibrating stability of the actuator is also demonstrated under a continuous operation for 30 min with a constant driving voltage of 500 V and frequency of 55 Hz. The velocity *vs.* time curves for the entire test period are stable, with peak values at 70 mm/s (less than 5% variations), as indicated in **Figure S25c and S25d**. The vibration displacements of cantilever configuration piezoelectret actuators with piezoelectret thickness of 150, 250, and 350 μm are measured by LDV and shown in **Figure S26**, proving that reducing the thickness is helpful to enhance the vibration intensity.

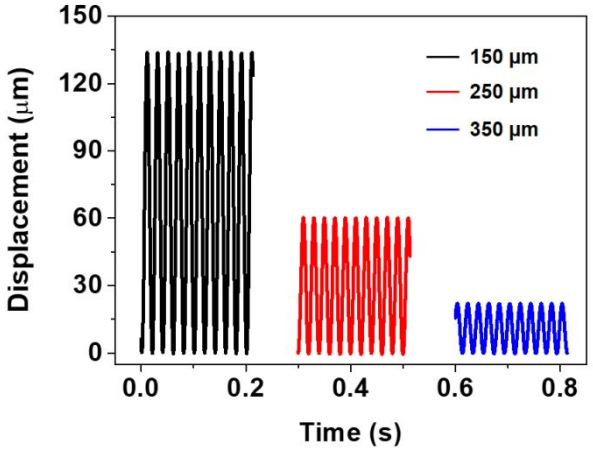

Figure S26. Vibration displacements of cantilever configuration piezoelectret actuators with piezoelectret thickness of 150, 250, and 350 μm, with driving voltage and frequency of 500 V and 50 Hz.

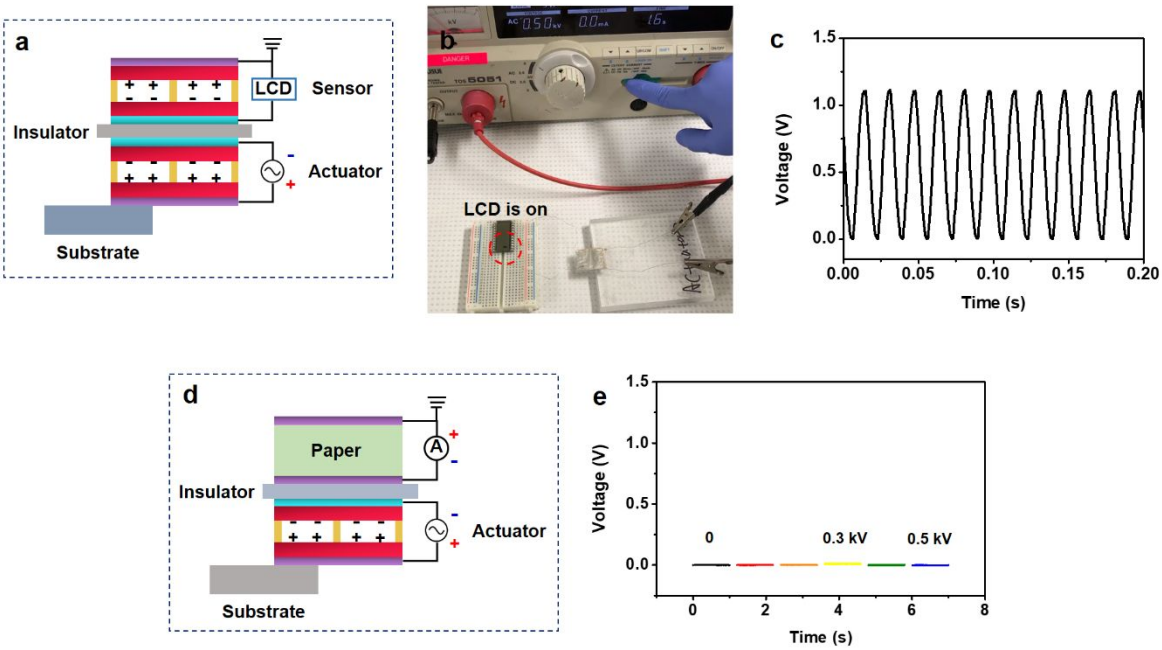

Figure S27. (a) Schematic diagram indicating that the vibration of the actuator with cantilever configuration can be measured by the sensor. (b) Photo image indicating that LCD is lit up by the sensor stimulated by the actuator. (c) The voltage-time curve across the LCD when the driving voltage and frequency of the actuator are 500 V and 60 Hz. (d) Actuator with cantilever configuration for stimulating paper piece with electrodes on both outside surfaces. (e) The measured voltage-time curves generated by the paper piece, under different applied voltage.

To further prove the vibration of cantilever configuration, a sensor and an actuator are integrated together, with an insulator between each other for preventing the direct contact (**Figure S27a**). The sensor can detect vibration generated by the actuator and the responding voltage-time signals are measured. When the driving voltage reaching 500 V, the peak values of the voltage is about 1.1 V (**Figure S27b**). The responding electricity of the sensor is strong enough to light up a pixel on the LCD, as indicted in **Figure S27c**. An actuator is also used to

stimulate a paper piece with electrodes on both outside surfaces (**Figure S27d**), and no obvious responding voltage signals are detected (**Figure S27e**), indicating that there is no electrical leakage issue.

Supplementary Explanation 2: An ideal and simplified model of a sandwich-structured piezoelectret patch as a sensor and its working mechanism.

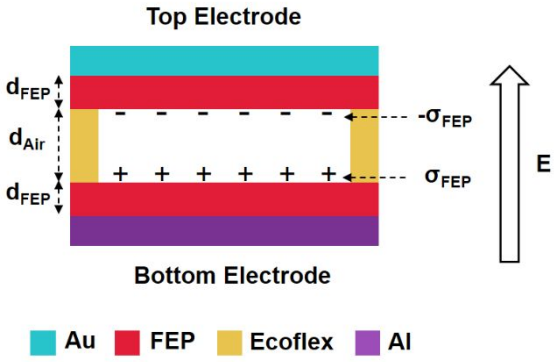

Figure S28. A simplified model of a sandwich-structured piezoelectret patch as a sensing unit (one working unit).

The simplified model of a sandwich-structured piezoelectret patch as a sensing unit is depicted in **Figure S28**. The sandwich-structured piezoelectret film consists of many FEP-air cavity-FEP structures in parallel. After the corona charging process, the inner surfaces of the FEP films are charged with opposite charges. We define the positive electric field direction to be from the bottom to the top. According to Gauss law:

$$\varepsilon_{\mathrm{FEP}} E_{FEP} - E_{air} = \frac{-\sigma_{FEP}}{\varepsilon_0} \tag{6}$$

Where ε_{FEP} is the dielectric constants of air and FEP film; ε_{FEP} is the permittivity of vacuum; E_{FEP} and E_{Air} represent the electric field in the FEP film and air cavity; σ_{FEP} represents the

charge density captured by the FEP inner surfaces.

According to Kirchhoff's second law under the short-circuit condition:

$$E_{FEP} = \frac{-\sigma_{FEP} d_{air}}{\varepsilon_0 (2d_{FEP} + \varepsilon_{FEP} d_{air})} \tag{7}$$

Where d_{Air} and d_{FEP} are the thickness of the FEP film and air cavity. As a result, the charge density on each electrode σ_e, is given by:

$$\sigma_e = -\varepsilon_{FEP}\varepsilon_0 E_{FEP} = \frac{\varepsilon_{FEP}\sigma_{FEP} d_{air}}{(2d_{FEP} + \varepsilon_{FEP} d_{air})} \tag{8}$$

In this case, all factors except d_{Air} are fixed. As such, σ_e is a function of d_{Air} (the thickness of the air cavity). As such, the gap thickness changes due to the external stimuli will affect σ_e to generating the electrical signals.

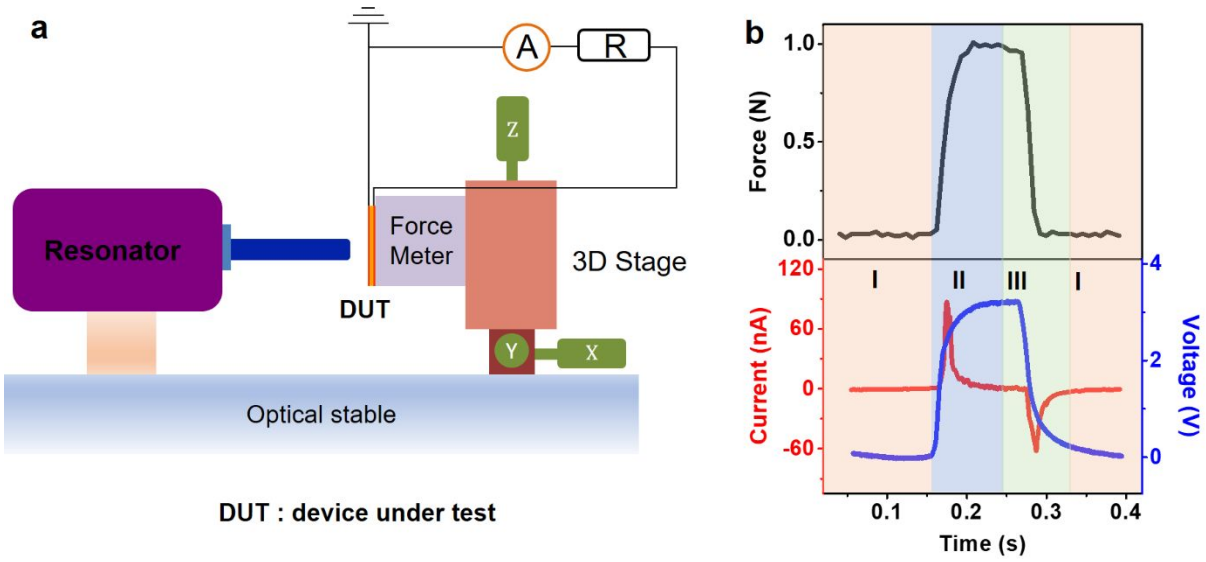

Figure S29. (a) The electrical measurement setup for a sandwich-structured piezoelectret patch as a sensor. (b) The external force is applied by a resonator (top) and the resulting short-circuit current and open-circuit voltage (bottom) measured by the sensor.

A force gauge with a 3D moving stage for tunable mechanical stimulations was utilized to characterize the sandwich-structured piezoelectret patch as a sensor, as given in **Figure S29a**.

Under an applied periodic force, the resulting open-circuit voltage and short-circuit current of the patch are recorded in **Figure. S29b**. In the initial state (Stage I), the electrical potential between the top and bottom electrodes is in an equilibrium state with no electrical outputs. Upon the mechanical compression (Stage II), the air gap thickness (d_{air}) is decreased and the induced charges on both electrodes decrease to result in a positive open-circuit voltage and a positive short-circuit current similar to a typical piezoelectric transducer. As the current drops to zero quickly (Stage II, red curve) as charge dissipates. When the force is released, d_{Air} can restore to its initial value due to the elasticity of the structure and the open-circuit voltage drops to zero, while the short-circuit current exhibits a sharp negative peak (Stage III). The process will repeat itself under the oscillating external stimuli.